BioSystems 203 (2021) 104373

Contents lists available at ScienceDirect

BioSystems

journal homepage: http://www.elsevier.com/locate/biosystems

# Electrical activity of fungi: Spikes detection and complexity analysis

Mohammad Mahdi Dehshibi [a,b,*], Andrew Adamatzky [b]

[a] Department of Computer Science, Multimedia and Telecommunications, Universitat Oberta de Catalunya, Barcelona, Spain
[b] Unconventional Computing Laboratory, University of the West England, Bristol, UK

ARTICLE INFO

*Keywords:*
Pleurotus djamor
Electrical activity
Spikes
Complexity

ABSTRACT

Oyster fungi *Pleurotus djamor* generate actin potential like spikes of electrical potential. The trains of spikes might manifest propagation of growing mycelium in a substrate, transportation of nutrients and metabolites and communication processes in the mycelium network. The spiking activity of the mycelium networks is highly variable compared to neural activity and therefore can not be analysed by standard tools from neuroscience. We propose original techniques for detecting and classifying the spiking activity of fungi. Using these techniques, we analyse the information-theoretic complexity of the fungal electrical activity. The results can pave ways for future research on sensorial fusion and decision making of fungi.

## 1. Introduction

Excitation is an essential property of all living organisms, bacteria Masi et al. (2015), Protists Eckert and Brehm (1979); Hansma (1979); Bingley (1966), fungi McGillviray and Gow (1987) and plants Trebacz et al. (2006); Fromm and Lautner (2007); Zimmermann and Mithöfer (2013) to vertebrates Hodgkin and Huxley (1952); Aidley and Ashley (1998); Nelson and Lieberman (2012); Davidenko et al. (1992). Waves of excitation could be also found in various physical Kittel (1958); Tsoi et al. (1998); Slonczewski (1999); Gorbunov and Kirsanov (1987), chemical Belousov (1959); Zhabotinsky (1964, 2007) and social systems Farkas et al. (2002, 2003). Extracellular (EC) action potential recordings have been widely used to record and measure neural activity in organisms with excitation. When recorded with differential electrodes, the spike manifests a propagating wave of excitation.

In our recent studies Adamatzky (2018b, 2019); Adamatzky et al. (2020), we have shown that the *Pleurotus djamor* oyster fungi generate action potentials like electrical potential impulses. We observed spontaneous spike[1] trains with two types of activity, i.e. high-frequency (2.6 min period) and low-frequency (14 min period). However, the proper use of this information is subject to the accurate extraction of the EC spike waveform, separating it from the background activity of the neighbouring cells and sorting the characteristics.

The lack of an algorithmic framework for the exhaustive characterisation of the electrical activity of the substrate colonised by mycelium of oyster fungi *Pleurotus djamor* has inspired us to develop a framework to extract spike patterns, quantify the diversity of spike events and measure the complexity of fungal electrical communication. We evidenced the spiking activity of the mycelium (see an example in Fig. 1), which will enable us to build an experimental prototype of fungi-based information processing devices.

We evaluated the proposed framework in comparison with existing spike detection techniques in neuroscience Nenadic and Burdick (2004); Shimazaki and Shinomoto (2010) and observed a significant improvement in the spike activity extraction. The evaluation of the proposed method for detecting spike events compared to the specified spike arrival time by the expert shows true-positive and false-positive rates of 76% and 16%, respectively. We found that the average dominant duration of an action-potential-like spike is 402 s. The amplitude of the spikes ranges from 0.5 mV to 6 mV and depends on the location of the source of electrical activity (the position of electrodes). We have found that the complexity of the Kolmogorov fungal spike ranges from $11 \times 10^{-4}$ to $57 \times 10^{-4}$. In Vicnesh and Hagiwara (2019), the human brain's Kolmogorov complexity is measured in normal, pre-ictal and ictal states resulting in 6.01, 5.59 and 7.12 values, respectively. Although the fungi' complexity is considerably smaller than that of the human brain, its changes suggest a degree of intra-communication in the mycelium sub-network. In fact, different parts of the substrate transmit different information to other parts of the mycelium network, where the more prolonged propagation of excitation waves leads to higher levels of

* Corresponding author. Department of Computer Science, Multimedia and Telecommunications, Universitat Oberta de Catalunya, Barcelona, Spain.
*E-mail addresses:* mdehshibi@uoc.edu, mohammad.dehshibi@yahoo.com (M.M. Dehshibi), andrew.adamatzky@uwe.ac.uk (A. Adamatzky).

[1] Calling the spikes spontaneous means that the intentional external stimulus does not invoke them. Otherwise, the spikes actually reflect the ongoing physiological and morphological processes in the mycelial networks.

https://doi.org/10.1016/j.biosystems.2021.104373
Received 20 October 2020; Received in revised form 23 January 2021; Accepted 24 January 2021
Available online 9 February 2021

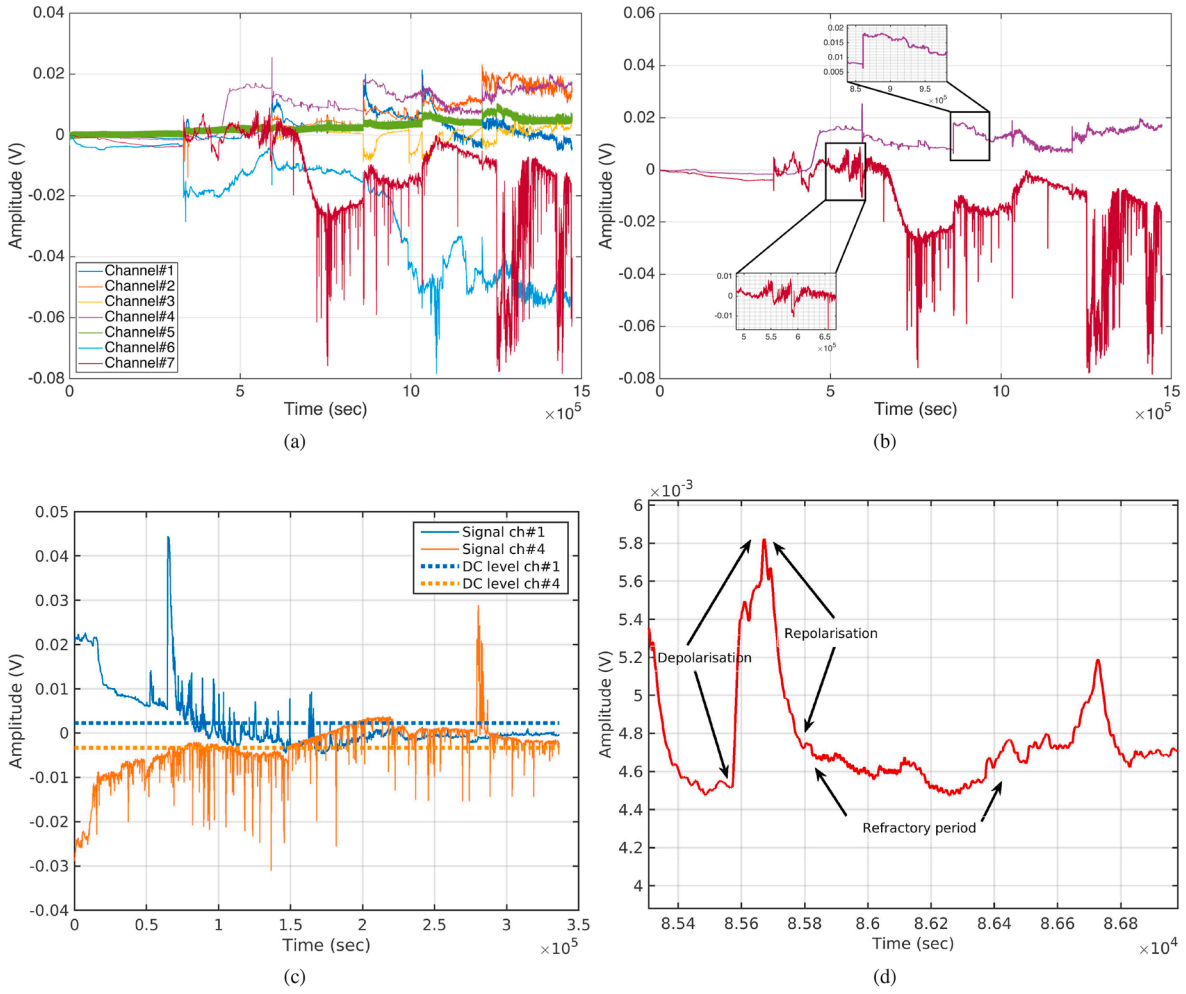


**Fig. 1.** The electrical behaviour of the mycelium of the grey oyster fungi. (a) Example of electrical potential dynamics recorded in seven channels of the same cluster during 409 h. (b) Two channels are zoomed in the inserts to show the rich combination of slow (hours) drift of base electrical potential combined with relatively fast (minutes) oscillations of the potential. (c) DC levelling for two channels is plotted. The mismatch of DC levels indicates the resistance and different levels of intra-communication in the substrate. (d) All 'classical' parts of the spike, i.e. depolarisation, depolarisation and refractory period, can be found in this sample spike. This spike has a length of 220 s, from the base-level potential to the refractory-like phase, and a refractory period of 840 s. The depolarisation and depolarisation rates are 0.03 and 0.009 mV/s, respectively.

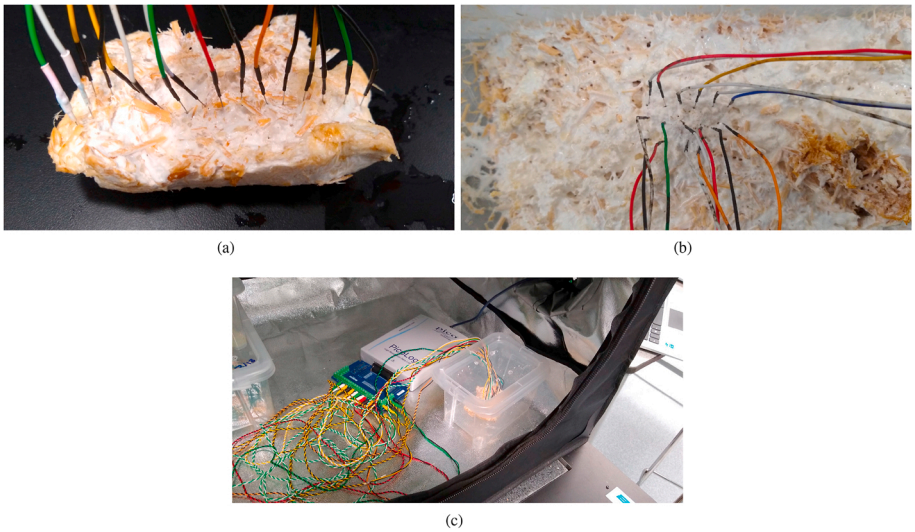


**Fig. 2.** (a) In-line placement of electrodes (1 cm distance), (b) random electrode placement, (c) the experimental setup.

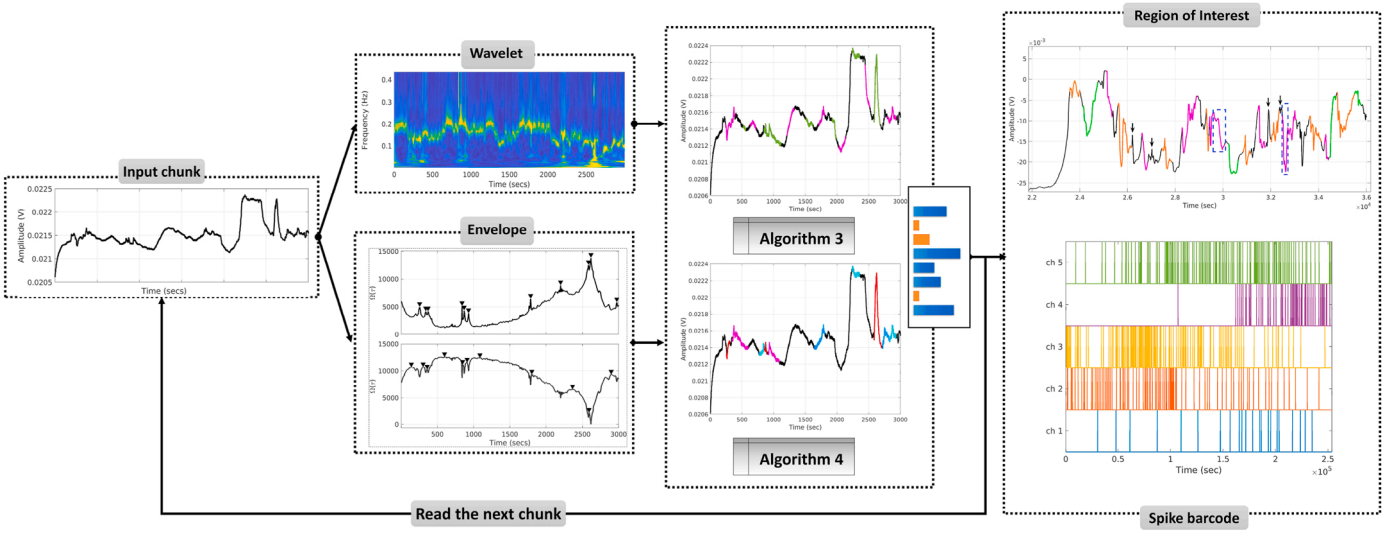


**Fig. 3.** The pipeline for the identification of spike events.

complexity.

The rest of this paper is structured as follows: Sect. 2 presents the experimental setup. Details of the proposed spike detection methods are explained in Sect. 3. Experimental results and complexity analyses are discussed in Sect. 4. Finally, the discussion is given in Sect. 5.

## 2. Experimental set-up

A wood shavings substrate was colonised by the mycelium of the grey oyster fungi, *Pleurotus ostreatus* (Ann Miller's Speciality Mushrooms Ltd, UK). The substrate was placed in a hydroponic growing tent with a silver Mylar lightproof inner lining (Green Box Tents, UK). Recordings were carried out in a stable indoor environment with the temperature remaining stable at $22 \pm 0.5^{\circ}$and relative humidity of air 40± 5%. The humidity of the substrate colonised by fungi was kept at c. 70–80%. Fig. 2 shows examples of the experimental setups.

We inserted pairs of iridium-coated stainless steel sub-dermal needle electrodes (Spes Medica SRL, Italy) with twisted cables into the colonised substrate for recording electrical activity. Using a high-resolution ADC-24 (Pico Technology, UK) data logger with a 24-bit A/D converter, galvanic insulation and software-selectable sample rates all lead to superior noise-free resolution. We recorded electrical activity one sample per second, where the minimum and maximum logging times were 60.04 and 93.45 h, respectively. During recording, the logger makes as many measurements as possible (basically up to 600 per second) and saves the average value. We set the acquisition voltage range to 156 mV with an offset accuracy of 9 μV at 1 Hz to preserve a gain error of 0.1%. Each electrode pair was considered independently with a 17-bit noise-free resolution and a 60 ms conversion time. In our experiments, electrode pairs were placed in one of two configurations: random placement or in-line placement. The distance between the electrodes was between 1 and 2 cm. In each cluster, we recorded 5–16 pairs of electrodes (channels) simultaneously.

In six trials, we also undertook recordings of the fruit body's resistance, where electrodes were inserted in stalks of the bodies. We measured and logged a range of resistances 1-1.6 kΩ using Fluke 8846A precision multimeter, where the test current being $1\pm 0.0013\mu$A, once per 10 s, $5 \times 10^4$ samples per trial Adamatzky et al. (2021). It should be noted that the placement of the electrodes in two experiments was in-lines with a distance of 1 cm, in two experiments it was in-lines with a distance of 2 cm, and in two experiments it was random with a distance of approximately 2 cm.

## 3. Proposed method

A spike event can be formally defined as an extracellular signal that exceeds a simple amplitude threshold and passes through a corresponding pair of user-specific time-voltage boxes. The spike, which involves depolarisation, depolarisation and refractory cycles, represents physiological and morphological processes in mycelial networks. To extract spike events, we proposed an unsupervised approach consisting of three major steps. The pipeline of the proposed approach is shown in Fig. 3.

- **Step 1:** We split the entire recording duration ($F(t)$) into $k$ chunks ($f_k(t)$) with respect to the signal transitions. In order to evaluate the transitions, we determined the state level of the signal by its histogram and identified all regions that cross the upper boundary of the low state and the lower boundary of the high state. Then, we measure scale-to-frequency conversions of the analytic signal in each chunk using Morse wavelet basis Lilly and Olhede (2012). To assess the existence of spike-like events, we scaled the wavelet coefficients at each frequency and obtained the sum of the scales below the threshold specified in Algorithm 1. Finally, we selected regions of interest (ROI) enclosed between a consecutive local minimum and a maximum of more than 30 s.
- **Step 2:** We used spline interpolation to measure the analytic signal envelopes around local maximum values. To determine the analytical signal, we first applied the discrete approximation of Laplace's differential operator to $f_k(t)$ to obtain a finite sequence of equally-spaced samples. Then, we applied discrete-time Fourier transform to this finite sequence. From the average signal envelope, we extracted regions spanning between a consecutive local minimum

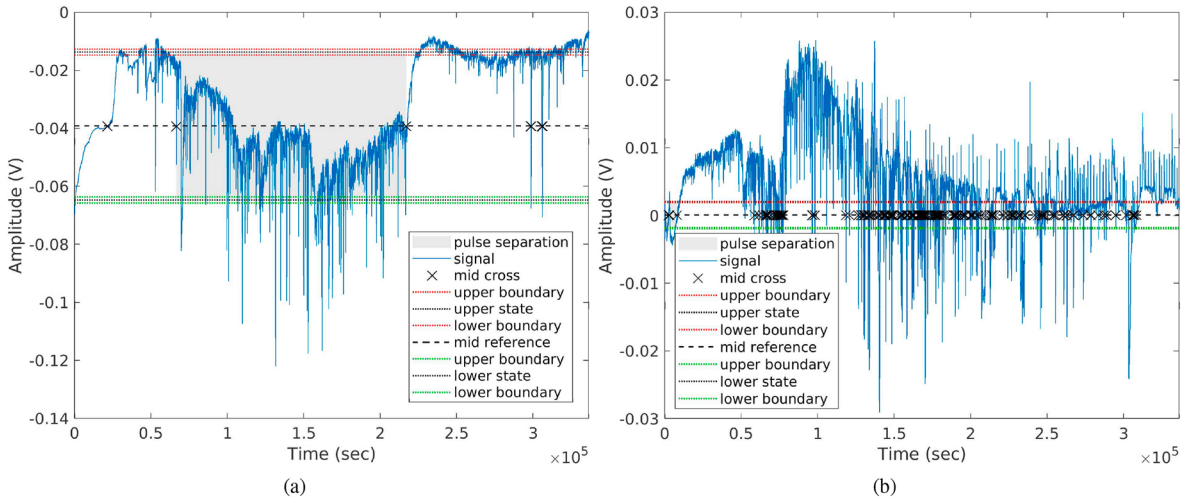


**Fig. 4.** Slicing electrical potential recordings for two channels.

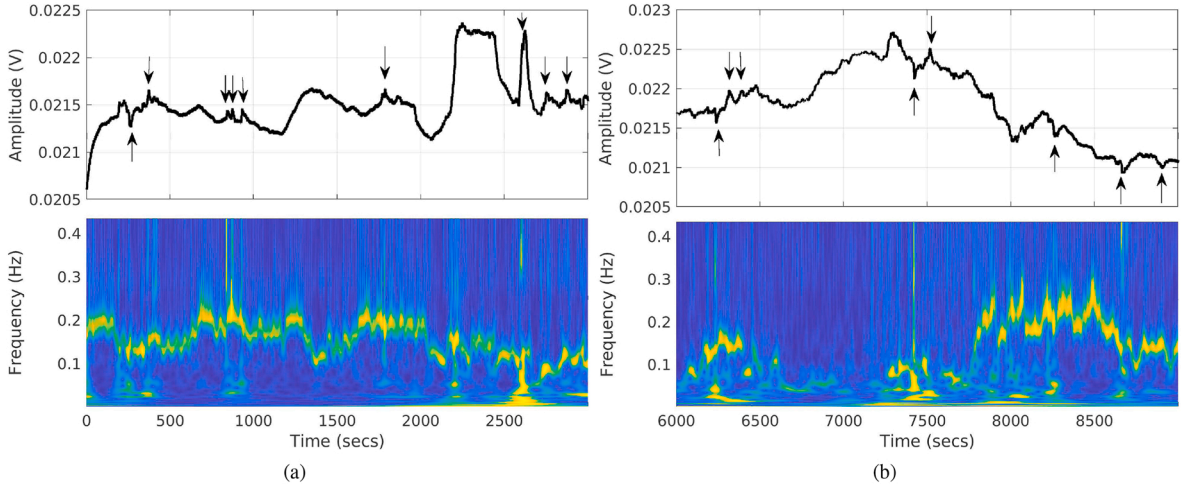


**Fig. 5.** Annotated spikes by the expert (black arrows) on the Morse wavelet scalogram for (a) $Slice_1$ and (b) $Slice_2$. The scalogram is plotted as a function of time and frequency, where the maximum absolute value at each frequency is used for the normalisation of the coefficient. The frequency axis is shown on a linear scale.

and a maximum. These regions created constraints that contributed to the identification of spike events.

– **Step 3:** We retained the ROIs extracted in the first step, which met the constraints of the second step. The signal envelope could direct wavelet decomposition in an unsupervised manner in order to cluster the signal into the spike, pseudo-spike, and background activity of the adjacent cells. In the following sub-sections, we detailed the proposed process.

### 3.1. Slicing fungi electrical activity

To split the electrical activity of fungi ($F(t)$) with a duration of ($t$) second into ($k$) chunks ($fk(t), 1 \leq k \leq t-1$), we used the signal transitions that constitute each pulse. To determine the transitions, we estimated the state level of $F(t)$ using the histogram method IEEE (2011). Then, we identified all regions that cross the upper boundary of the low state and the lower boundary of the high state. We followed the following steps to estimate the signal states:

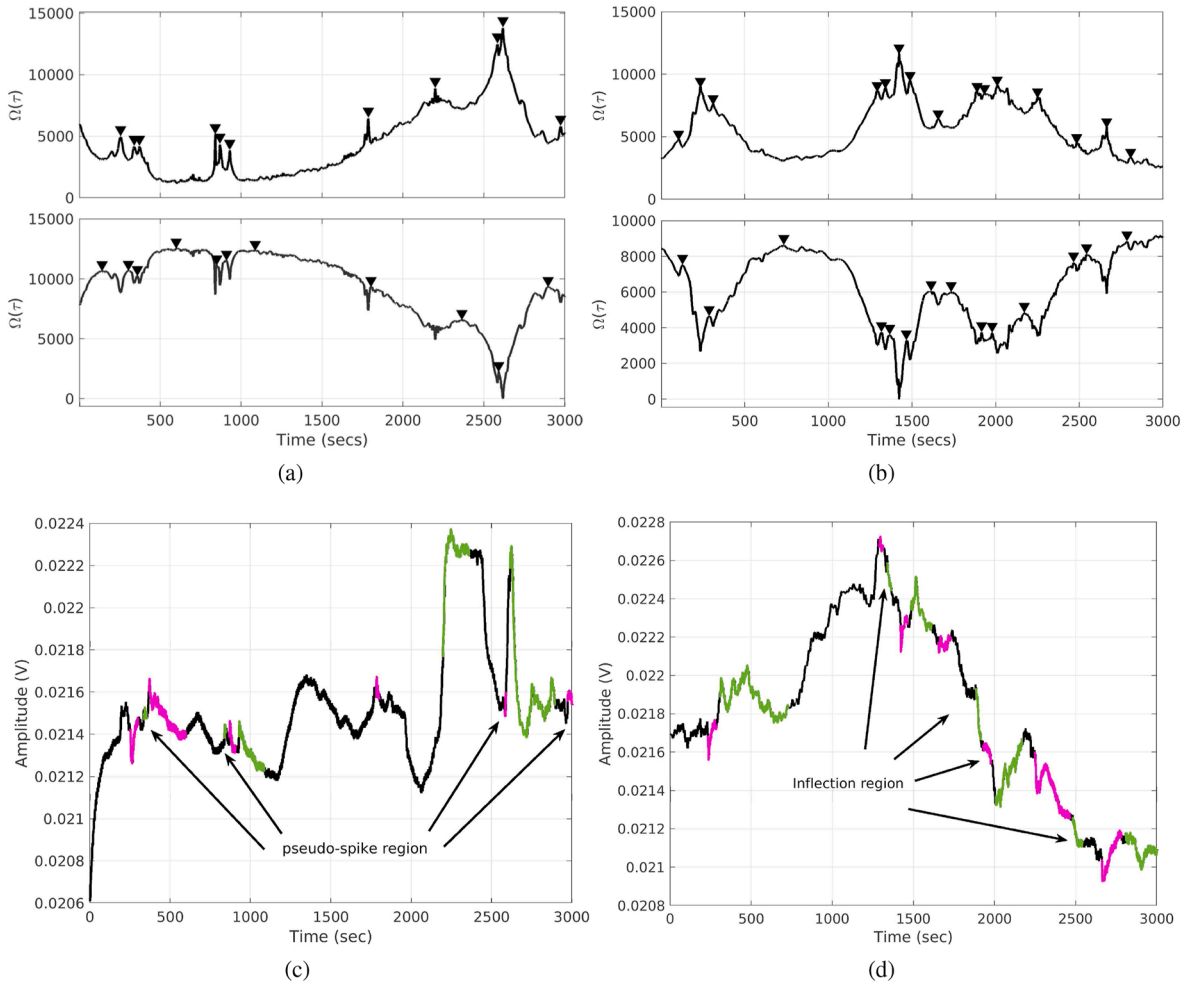


**Fig. 6.** (a,b) Identified local maxima and minima over $g_{\beta,\gamma}(\tau,s)$ in (a) *Slice*$_1$ and (b) *Slice*$_2$. The second-row of the plot is the inverse of the first row; therefore, the marked maximums are identical to the local minima. (c,d) Candidate regions of interest which are alternately coloured purple and green to ease visual tracking.

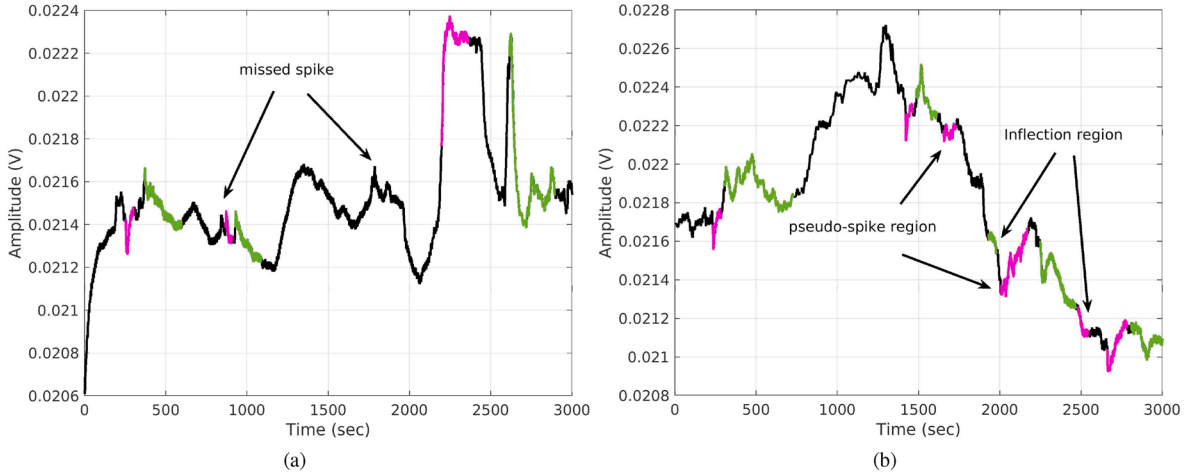


**Fig. 7.** Results of applying Algorithm 2 to (a) *Slice*$_1$ and (b) *Slice*$_2$. Two spike events are missed in *Slice*$_1$. Two pseudo-spike and two inflection regions still remain in *Slice*$_2$.

1. Determine the minimum, maximum and range of amplitudes.
2. Sort the amplitude values in the histogram bins and determine the width of the bin by dividing the amplitude range by the number of bins.
3. Identify the lowest- and highest-indexed histogram bins, $hb_{low}$, $hb_{high}$, with non-zero counts.
4. Divide the histogram into two sub-histograms, where the indices of the lower and upper histogram bins are $hb_{low} \leq hb \leq \frac{1}{2}(hb_{high} - hb_{low})$ and $hb_{low} + \frac{1}{2}(hb_{high} - hb_{low}) \leq hb \leq hb_{high}$, respectively.
5. Calculate the mean of the lower and upper histogram to compute the state levels.

Each chunk is then enclosed between the last negative-going transitions of each positive-polarity pulse and the next positive-going transition. Fig. 4 shows the slicing results of two channels.

### 3.2. Detecting time-localised events by Morse-based wavelets

The electrical activity of mycelium shows modulated behaviour with changes in amplitude and frequency over time. This feature suggests that the signal can be analysed with analytic wavelets, which are naturally grouped into pairs of even or cosine-like and odd or sine-like pairs, allowing them to capture phase variability. A wavelet ($\psi(t)$) is a finite energy function that projects $f(t)$ to a family of time-scale waveforms through translation and scaling. The Morse wavelet ($\psi_{\beta,\gamma}(t)$) is an analytical wavelet whose Fourier transform is supported only on a positive real axis Lilly and Olhede (2012); Lilly (2017). This wavelet is defined in the frequency domain using Eq. (1).

$$\psi_{\beta,\gamma}(t) = \frac{1}{2\pi}\int_{-\infty}^{\infty} \Psi_{\beta,\gamma}(\omega)\, e^{i\omega t}\, \mathrm{d}\omega,$$

$$\Psi_{\beta,\gamma}(\omega) \equiv \begin{cases} a_{\beta,\gamma}\omega^{\beta} e^{-\omega^{\gamma}} & \omega > 0 \\ \frac{1}{2}\left(a_{\beta,\gamma}\omega^{\beta} e^{-\omega^{\gamma}}\right) & \omega = 0 \cdot \\ 0 & \omega < 0 \end{cases} \tag{1}$$

where $\beta \geq 0$ and $\gamma > 0$, ω is the angular frequency and $a_{\beta,\gamma} \equiv 2\left(\frac{e\gamma}{\beta}\right)^{\frac{1}{\gamma}}$ is the amplitude coefficient used as a real-valued normalised constant. Here, $e$ is Euler's number, β characterises the low-frequency behaviour, and γ defines the high-frequency decay. We can rewrite Eq. (1) in the Fourier domain, parameterised by β and γ as in Eq. (2).

$$\varphi_{\beta,\gamma}(\tau, s) \equiv \int_{-\infty}^{\infty} \frac{1}{s}\, \psi^{*}_{\beta,\gamma}\left(\frac{t-\tau}{s}\right) f(t)\, \mathrm{dt} = \frac{1}{2\pi}\int_{-\infty}^{\infty} \mathrm{e}^{\mathrm{i}\omega\tau}\, \Psi^{*}_{\beta,\gamma}(\mathrm{s}\omega)\mathrm{F}(\omega)\, \mathrm{d}\omega. \tag{2}$$

where $F(\omega)$ is the Fourier transform of $f(t)$, and * denotes the complex conjugate. When $\Psi^{*}_{\beta,\gamma}(\omega)$ is real-valued, the conjugation may be omitted. The scale variable $s$ allows the wavelet to stretch or compress in time. In order to reflect the energy of $f(t)$ and to normalise time-domain wavelets to preserve constant energy, $\frac{1}{\sqrt{s}}$ is typically used. However, instead, we used $\frac{1}{s}$ since we define the amplitude of the time-located signals. To recover time-domain representation, we can use the inverse Fourier transform by $f(t) = \frac{1}{2\pi}\int_{-\infty}^{\infty} e^{i\omega t} F(\omega)\, \mathrm{d}\omega$ and $\psi_{\beta,\gamma}(t) = \int_{-\infty}^{\infty} e^{i\omega t}\, \mathrm{dt} = 2\pi\delta(\omega)$, where $\delta(\omega)$ is the Dirac delta function.

The representation of Morse wavelets would be more oscillatory when both β and γ increase, and more localised with impulses when these parameters decrease. On the other hand, increasing β and holding γ fixed expand the central portion of the wavelet and increase the long-term rate of decay. Whereas, increasing γ by keeping β constant extends the wavelet envelope without affecting the long-term decay rate. Inspired by Lilly and Olhede (2008), we set the symmetry parameter γ to 3 and the time-bandwidth product $P^2 = \beta\gamma$ to 60. We have used $L_1$ normalisation to provide the same magnitude in wavelets when we have the same amplitude oscillatory components at different scales.

Fig. 5 displays two randomly chosen 3000-s chunks of fungi electrical activity (namely $Slice_1$ and $Slice_2$) with their Morse wavelet scalograms. We observed that the use of the maximum absolute value at each frequency (level) to normalise coefficients may help to identify events that may involve spikes. We then used Eq. (3) to normalise coefficients and set zero entries to 1.

$$\kappa_{\beta,\gamma}(\tau, s) = \left|\varphi_{\beta,\gamma}(\tau, s)\right|^{\intercal},$$

$$g_{\beta,\gamma}(\tau, s) = \left(\eta \times \frac{\kappa_{\beta,\gamma}(\tau, s) - \min_s\left(\kappa_{\beta,\gamma}(\tau, s)\right)}{\max_s\left(\kappa_{\beta,\gamma}(\tau, s)\right)}\right)^{\intercal}. \tag{3}$$

where $|\bullet|$ and $(\bullet)^{\intercal}$ return the absolute value and the matrix transpose, respectively. Here, η is a scaling factor that we empirically set to 240. We used $g_{\beta,\gamma}(\tau, s)$ in Algorithm 1 to extract the candidate ROIs shown in Fig. 6. As shown in Fig. 6(c and d), some of the detected regions are either too short[2] or lack repolarisation and depolarisation periods that should be removed from $\mathscr{B}$.

Algorithm 2 is proposed to eliminate so-called pseudo-spike and inflection regions which do not reach the spike characteristics as shown in Fig. 7. Applying Algorithm 2 resulted in the loss of two spikes in $Slice_1$ (see Fig. 7(a)) and the failure to eliminate two pseudo-spike and two inflection regions in $Slice_2$ (see Fig. 7(b)). We found that the analysis of the analytic signal by its envelope could improve the accuracy of the spike detection.

### 3.3. Analytical signal envelope for locating spike pattern

We calculated the magnitude of the analytic signal to obtain the signal envelope (ξ). The analytic signal is detected using the discrete Fourier Transform as implemented in the Hilbert Transform. In order to highlight effective signal peaks and neutralise *inflection* regions, the second numerical signal derivation ($L = \partial^2 f / 4\partial t^2$) was calculated. A frequency-domain approach is proposed in Marple (1999) to approximately generate a discrete-time analytic signal. In this approach, the negative frequency in half of each spectral period is set to 0, resulting in a periodic one-sided spectrum. The procedure for generating a complex-valued $N$-point ($N$ is even) discrete-time analytic signal ($F(\omega)$) from a real-valued $N$-point discrete time signal ($L[n]$) is as follows:

1. Calculate the $N$-point discrete-time Fourier transform using $F(\omega) = T\sum_{n=0}^{N-1} L[n]e^{-i2\pi\omega Tn}$, where $|\omega| \leq 1/2T$ Hz. $L[n]$ , $0 \leq n \leq N-1$ is obtained by sampling the band-limited real-valued continuous-time signal $L(nT) = L[n]$ at periodic time intervals of $T$ seconds to prevent aliasing.
2. Calculate the $N$-point one-sided discrete-time analytic signal transform:

$$Z[m] = \begin{cases} F[0], & \text{for } m = 0 \\ 2F[m], & \text{for } 1 \leq m \leq \frac{N}{2} - 1 \\ F\left[\frac{N}{2}\right], & \text{for } m = \frac{N}{2} \\ 0, & \text{for } \frac{N}{2} + 1 \leq m \leq N - 1. \end{cases} \tag{4}$$

3. Calculate the $N$-point inverse discrete-time Fourier transform to obtain the complex discrete-time analytic signal of same sample rate as the original $L[n]$

$$z[n] = \frac{1}{NT}\sum_{m=0}^{N-1} Z[m] e^{\frac{i2\pi mn}{N}} \tag{5}$$

[2] We observed in our previous studies Adamatzky (2018b, 2019) that minimum spike length was 5 min.

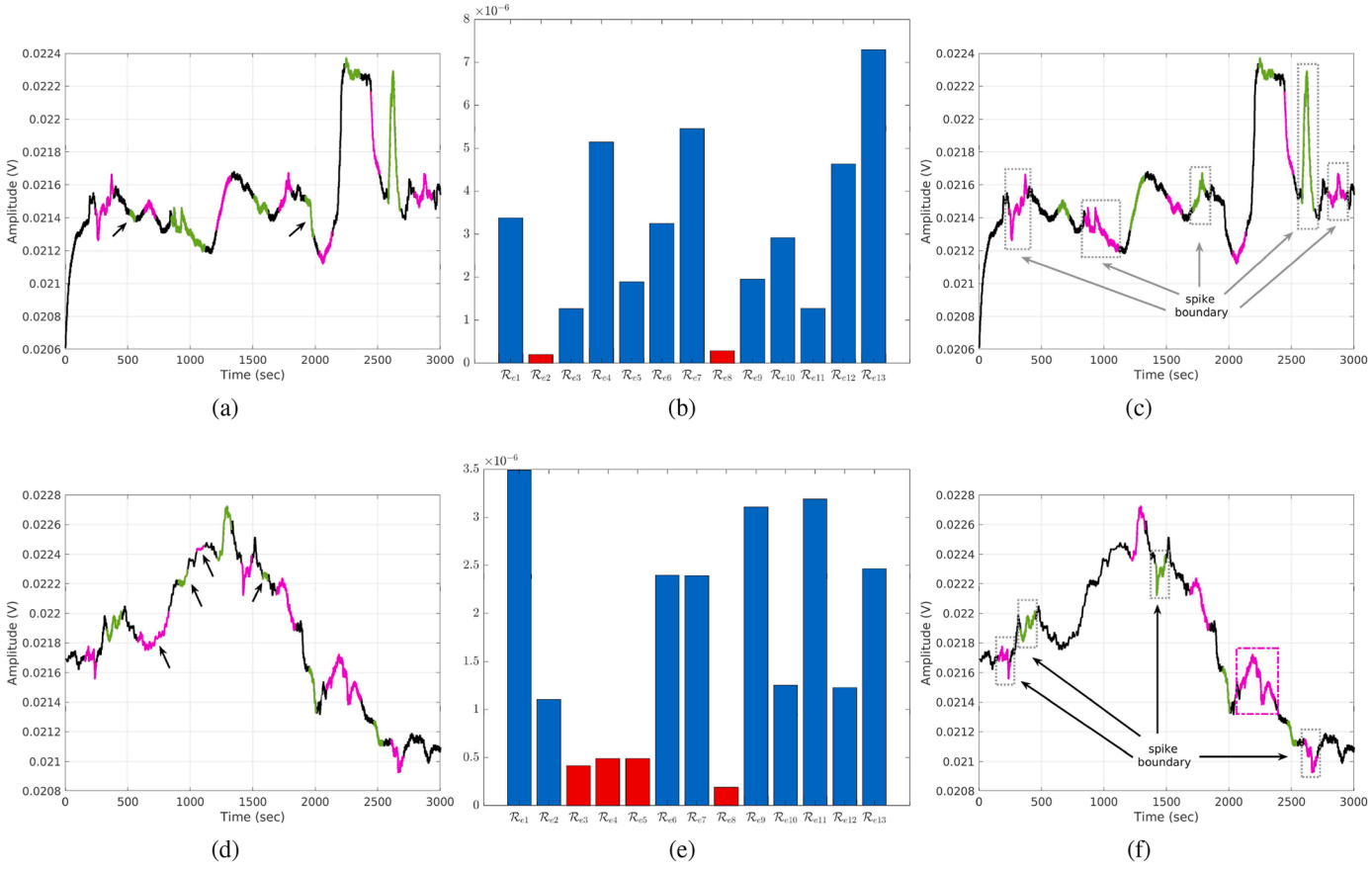


**Fig. 8.** Results of Algorithm 3 applied to $Slice_1$ (first row) and $Slice_2$ (second row). (a,d) Candidate regions by finding local minima and maxima in the analytic signal envelope. The pointed regions are also highlighted in the bar chart in red. (b,e) The absolute difference in prominence between the successive local minima and maxima. Regions that do not satisfy $\mathscr{R}_3(k) < \rho$ are coloured in red. (c,f) Regions of Interest in $\mathscr{R}$. The grey dashed rectangle shows the correct spike, including repolarisation, depolarisation, and refractory periods. The purple dashed rectangle shows the region whose refractory period attached to the pseudo-spike region.

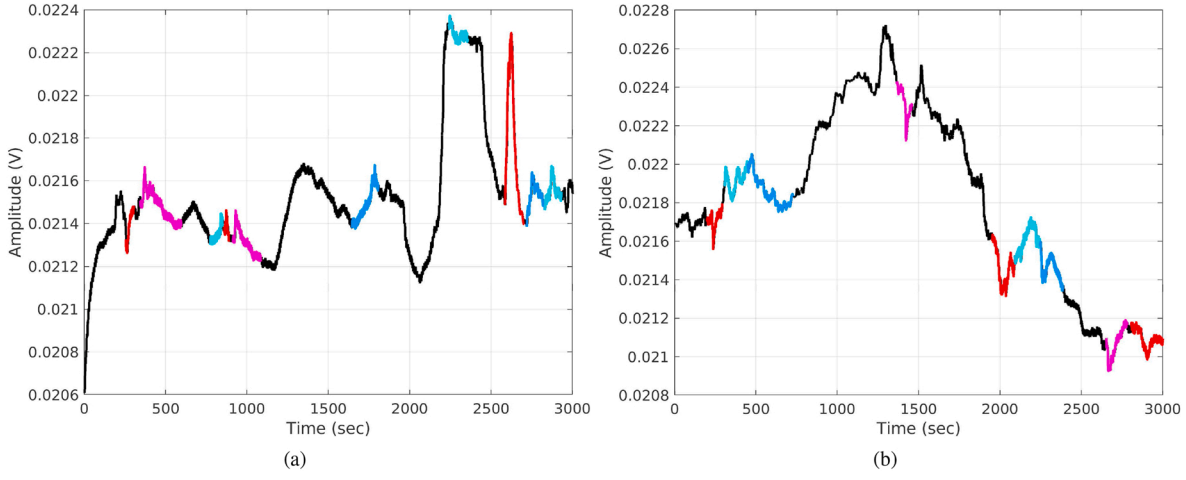


**Fig. 9.** Results of applying Algorithm 4 to (a) $Slice_1$ and (b) $Slice_2$. We alternatively used red/purple for colouring spike events and blue/cyan for colouring pseudo-spike events.

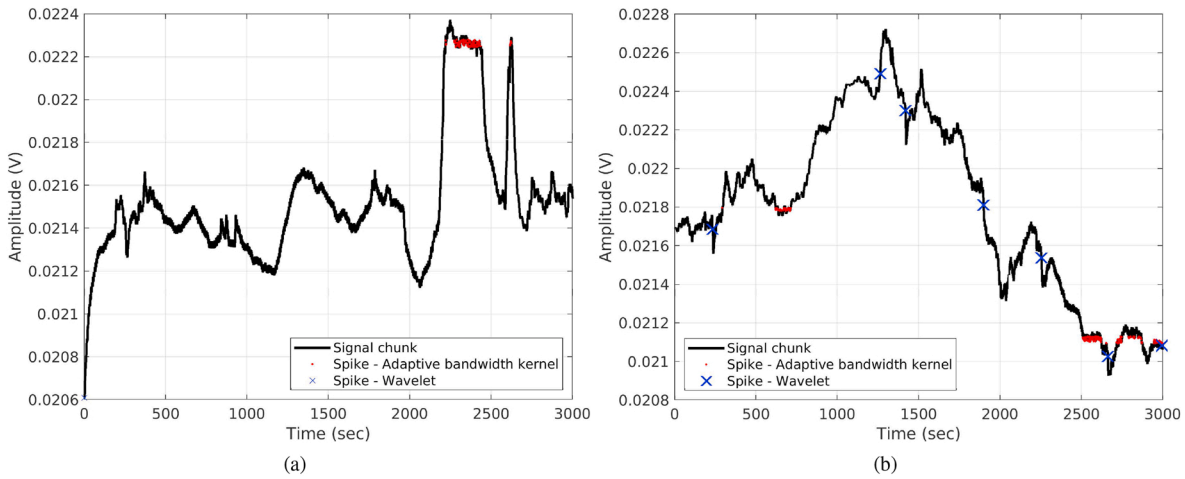


**Fig. 10.** Results of applying proposed algorithms in Nenadic and Burdick (2004); Shimazaki and Shinomoto (2010) to (a) $Slice_1$ and (b) $Slice_2$. Note that the wavelet-based method can only locate spike arrival time. The kernel bandwidth optimisation can, however, extract the spike region.

**Algorithm 1**. Detecting candidate regions for time-localised events.

**Algorithm 1:** Detecting candidate regions for time-localised events.

**Input :** $g_{\beta,\gamma}(\tau, s)$ – Scaled wavelets coefficients.
**Output:** $\mathcal{B}$ – set of candidate regions.

**begin**
  $\epsilon = 0.05 \times (\max(g_{\beta,\gamma}(\tau, s)) - \min(g_{\beta,\gamma}(\tau, s)))$;
  $max_g \leftarrow$ set of all `LocalMaximum`$(g_{\beta,\gamma}(\tau, s), \epsilon)$;
  `//` `LocalMaximum()` `returns` $\tau^*$ `if` $\forall \tau \in (\tau^* \pm \epsilon),\ g_{\beta,\gamma}(\tau^*, s) \geq g_{\beta,\gamma}(\tau, s)$.
  $min_g \leftarrow$ set of all `LocalMinimum`$(g_{\beta,\gamma}(\tau, s), \epsilon)$;
  $\mathcal{U} \leftarrow$ **sort**$(min_g \bigcup max_g)$;
  $n =$ **card**$(\mathcal{U})$;
  `//` **card**$(A)$ `returns number of entries in` $A$.
  **if** $n \equiv 1 \pmod 2$ **then**
    slack $\leftarrow$ **mean**(difference of two consecutive entries);
    Add **min**$(\mathcal{U}_n +$ slack$, \tau)$ to $\mathcal{U}$;
    $n = n + 1$;
  **end**
  $\mathcal{B} \leftarrow (\mathcal{U}_i, \mathcal{U}_{i+1}),\ \forall i \in \{1, 3, \cdots, n-1\}$
**end**
**return** $\mathcal{B}$

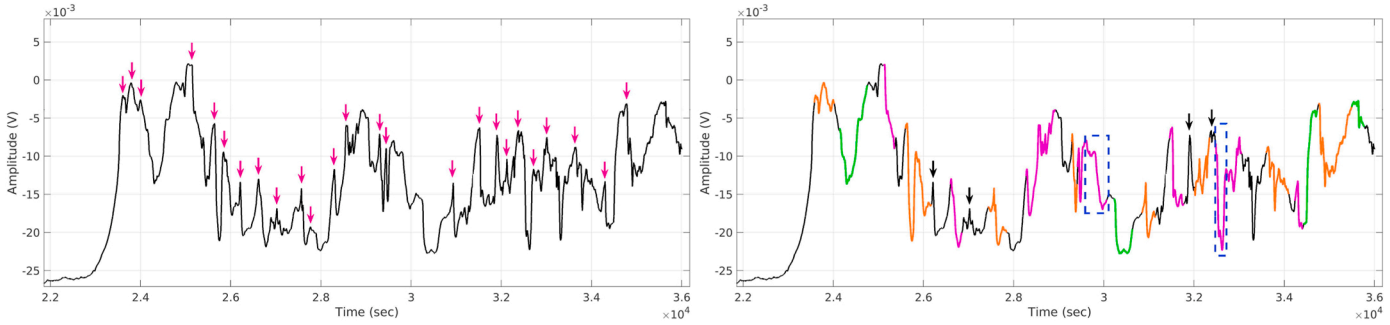


**Fig. 11.** (a) Spike arrival time located by the expert. Here we used augmented pink arrow to point to these spikes. (b) Spike regions extracted by the proposed method. Spike regions are alternatively coloured in orange and violet. The green areas point to *pseudo-spike* regions that are mistaken for spikes. Blue rectangles with dash edge show overestimated refractory periods. We used black arrows to point to the missed spikes.

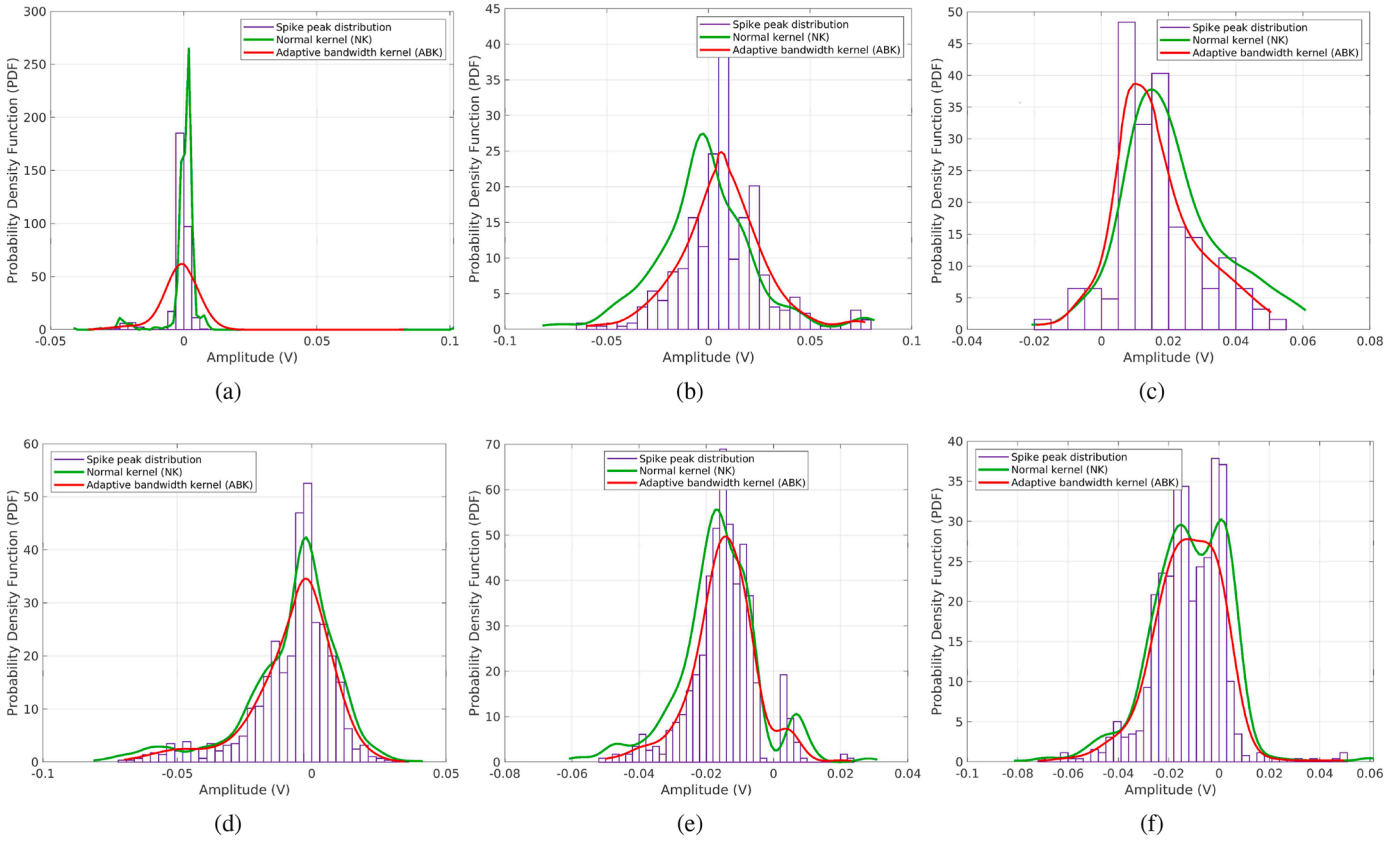


**Fig. 12.** Distribution of spike event lengths with superimposed Gaussian and Adaptive bandwidth kernels Shimazaki and Shinomoto (2010). (a,b) In-line electrode arrangements with a distance of 1 cm. (c,d) In-line electrode arrangements with a distance of 2 cm. (e,f) Random electrode arrangements with an approximate distance of 2 cm.

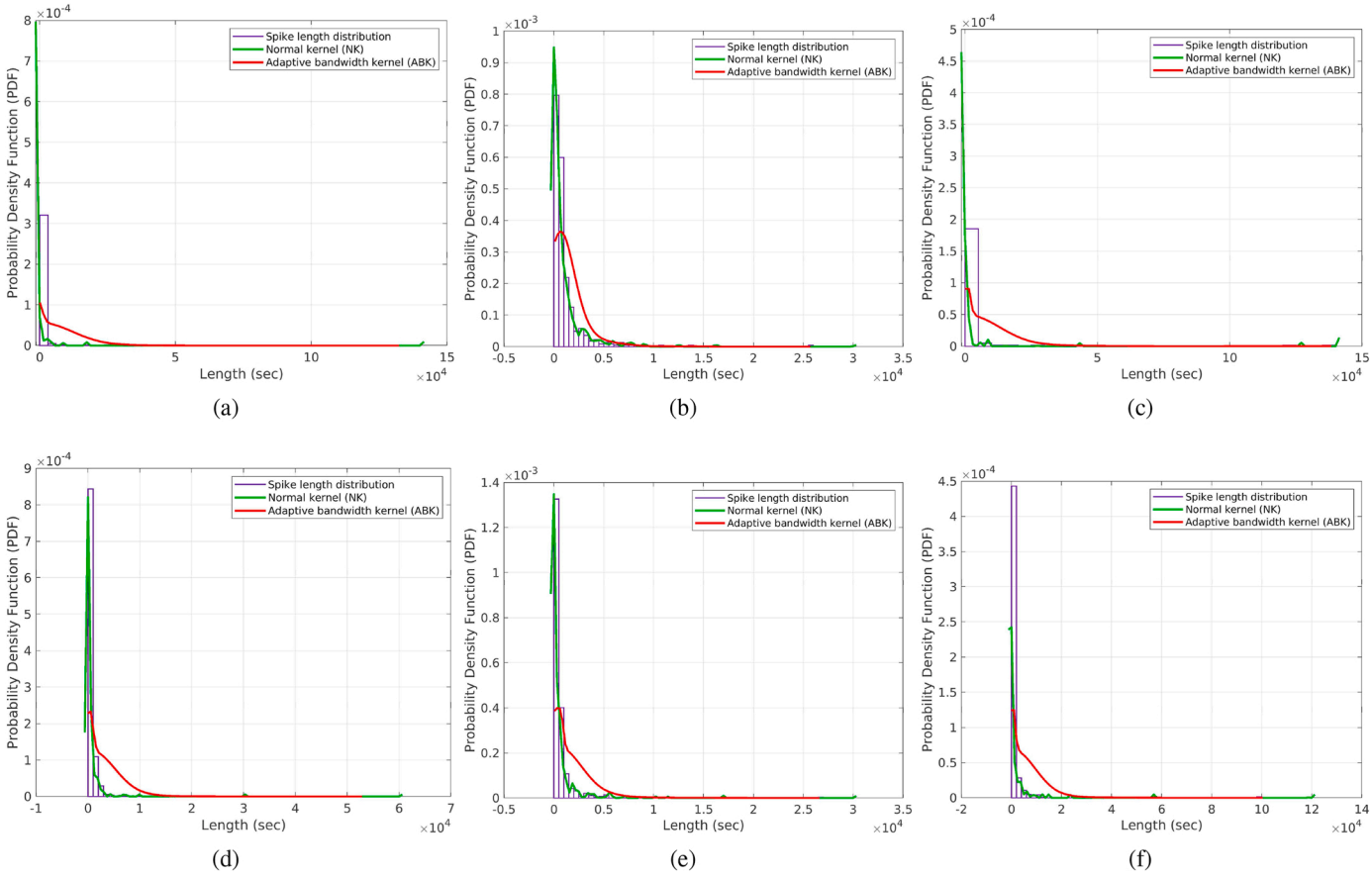


**Fig. 13.** Distribution of spike maximum amplitudes with superimposed Gaussian and Adaptive bandwidth kernels Shimazaki and Shinomoto (2010) for (a,b) in lines electrode placement with a distance of 1 cm. (c,d) in lines electrode placement with a distance of 2 cm. (e,f) random electrode placement with an approximate distance of 2 cm.

**Table 1**
The dominant value and bandwidth for the length and amplitude of the spike in each experiment across all recording channels. Duration and amplitude of spikes are estimated by the probability density function (PDF) and the adaptive bandwidth kernel (ABK) Shimazaki and Shinomoto (2010). The bold-faced **blue** and **red** entries show the absolute minimum and maximum values, respectively. As we have bi-directional potential changes, we have considered absolute value.

| | #Channels | #Spikes | Length (sec) | | | | Amplitude (V) | | | |
|---|---|---|---|---|---|---|---|---|---|---|
| | | | PDF | | ABK | | PDF | | ABK | |
| | | | Dominant | Bandwidth | Dominant | Bandwidth | Dominant | Bandwidth | Dominant | Bandwidth |
| #1 | 8 | 565 | **84.00** | 75.61 | **84.00** | 60.22 | **0.00003** | 0.00048 | **-0.00117** | 0.00576 |
| #2 | 5 | 447 | 366.80 | 154.31 | 625.60 | 126.47 | 0.00642 | 0.00544 | 0.00642 | 0.00667 |
| #3 | 4 | 124 | 84.00 | 75.61 | 84.00 | 60.22 | 0.00003 | 0.00048 | -0.00117 | 0.00576 |
| #4 | 5 | 951 | 534.12 | 80.09 | 534.12 | 84.80 | -0.00239 | 0.00301 | -0.00239 | 0.00508 |
| #5 | 5 | 573 | 334.25 | 74.52 | 334.25 | 80.9 | **-0.01536** | 0.00218 | **-0.01462** | 0.00357 |
| #6 | 15 | 862 | **1014.72** | 99.53 | **1014.72** | 92.67 | -0.00172 | 0.00381 | -0.01277 | 0.00591 |

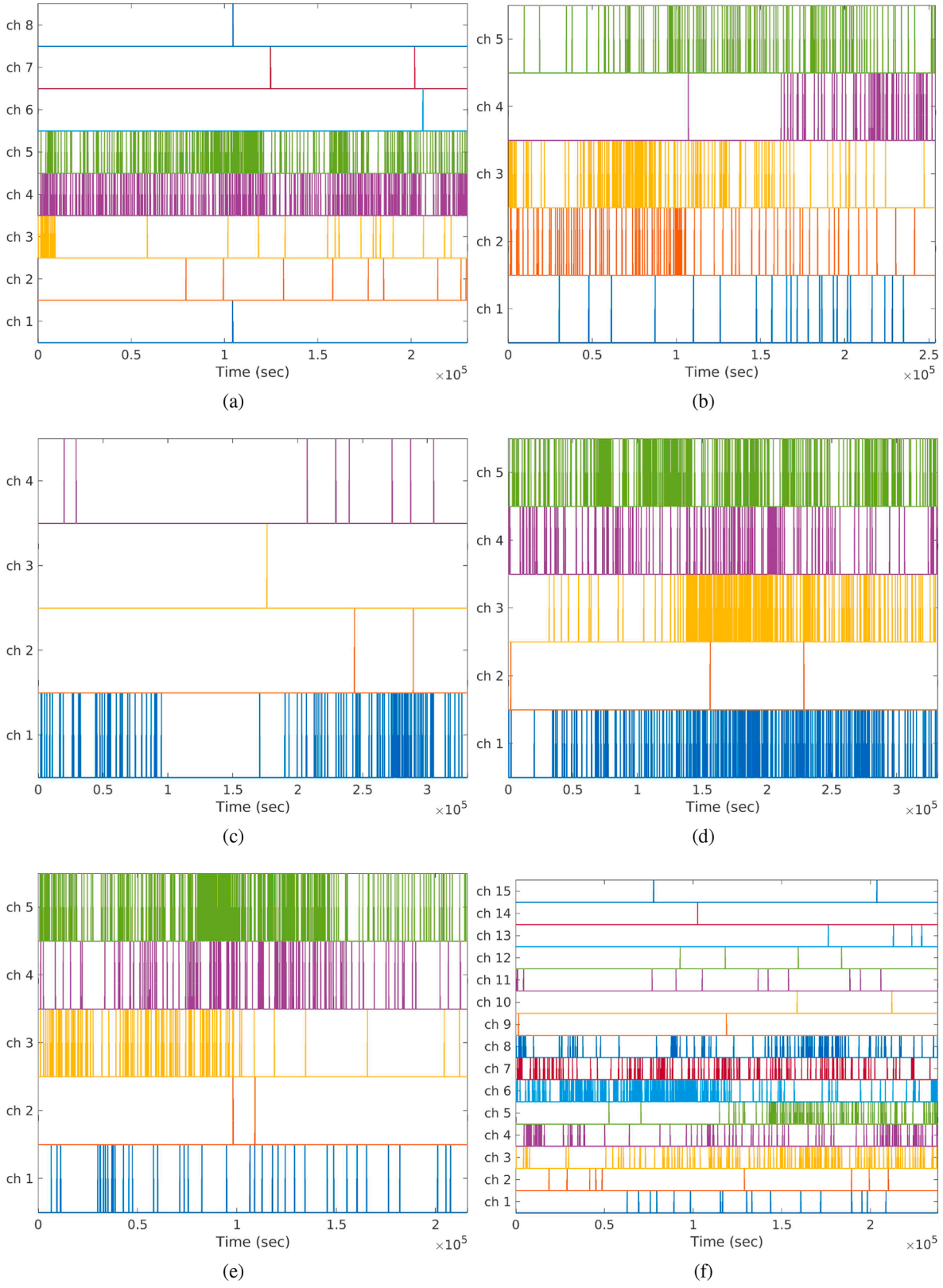


**Fig. 14.** Barcode-like representation of spike events in various channels for (a,b) in-line electrode arrangements at a distance of 1 cm, (c,d) in-line electrode arrangements at a distance of 2 cm, and (e,f) random electrode arrangements at an approximate distance of 2 cm.

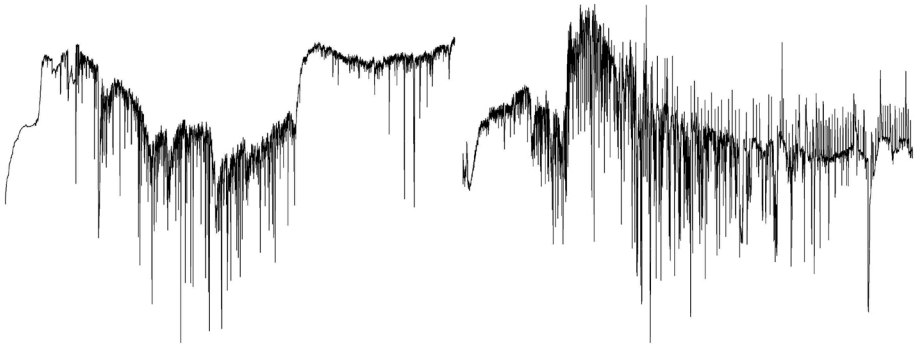


**Fig. 15.** Two samples from input channels, which are saved in black and white PNG format without axes and annotations.

**Algorithm 2.** Excluding pseudo-spike and inflation regions form candidate ROI (Hall and Meyer, 1976).

**Algorithm 2:** Excluding pseudo-spike and inflation regions form candidate ROI.

**Input :** $\mathcal{B}$ — set of ROI, *i.e.*, Algorithm 1 output,
$f$ — Electrical potential.
**Output:** $\mathcal{C}$ — set of wavelet-based ROIs,
$\mathcal{D}$ — set of *pseudo-spike* and *inflection* regions.

**begin**
  **for** $i = 1$ **to card**$(\mathcal{B})$ **do**
    $lb \leftarrow \mathcal{B}(i, 1)$;
    $ub \leftarrow \mathcal{B}(i, 2)$;
    **if** $(ub - lb) > 30$ **then**
      $chunk = f[lb \cdots ub]$;
      $minima =$ **min**(`isLocalMinimum(`$chunk$`)`);
      `// isLocalMinimum() and isLocalMaximum() use spline interpolation in locating local extreme Hall and Meyer (1976).`
      $maxima =$ **max**(`isLocalMaximum(`$chunk$`)`);
      **if** $f(minima) <$ **min**$(f(lb), f(ub))$ **or** $f(maxima) >$ **max**$(f(lb), f(ub))$ **then**
        $\mathcal{C} \leftarrow [lb, ub]$;
      **else**
        $\mathcal{D} \leftarrow [lb, ub]$;
      **end**
    **end**
  **end**
**end**
**return** $\mathcal{C}$, $\mathcal{D}$

Obtaining an analytic signal in this way satisfies two properties: (1) The real part is equivalent to the original discrete-time sequence; (2) the real and imaginary components are orthogonal. Calculating the magnitude of the analytic signal using Eq. (6) results in the signal envelope ($\xi[n]$) containing the upper ($\xi_H[n]$) and lower ($\xi_L[n]$) envelopes of $L[n]$.

$$\xi[n] = |z[n]| \tag{6}$$

Envelopes are calculated using spline interpolation over a local maximum separated by at least $n_p = 60$ samples. We considered $n_p = 60$ because, in our previous studies Adamatzky (2018b, 2019), we did not observe any electrical potential of spikes shorter than 60 s. Algorithm 3 was proposed to locate candidate regions using a signal envelope.

Fig. 8 (a,d) shows the candidate regions in $\mathscr{R}$ before applying Step 13. At this step, while $\mathscr{R}$ includes regions that do not align with the spike definition (pointed by arrow in the plot), the correctly identified spikes are consistent with our findings in Adamatzky (2018a, b). Steps 13 and 14 were used to remove non-spike regions marked in red in Fig. 8 (b,e). However, the output of Algorithm 3 (see Fig. 8 (c,f)) still includes regions belonging to either *pseudo-spike/inflection* regions or refractory periods attached to pseudo-spike regions.

To fix mis-identified ROIs in Algorithms 2 and 3, we proposed Algorithm 4 in which regions in $(\mathscr{C} \cup \mathscr{D})$ are used to update $\mathscr{R}$. Indeed, if the ROI in $\mathscr{R}$ is a subset of $(\mathscr{C} \cup \mathscr{D})$, we add it to the spike event set ($\mathscr{T}_s$) and update the spike length. If the ROI in $(\mathscr{C} \cup \mathscr{D})$ is a subset of $\mathscr{R}$, we add it to the pseudo-spike set ($\mathscr{T}_p$). In the case of an intersection that does not meet the subset requirement, we concatenate ROIs and divide the new region from the intersection point into two segments. Then, we add the segment with the minimum length to $\mathscr{T}_p$. Finally, regions with a length of less than 60 s are excluded from both $\mathscr{T}_s$ and $\mathscr{T}_p$. The results are shown in Fig. 9.

## 4. Experimental results

This section consists of objective and complexity analyses. In the objective analysis, we demonstrated the effectiveness of the spike event

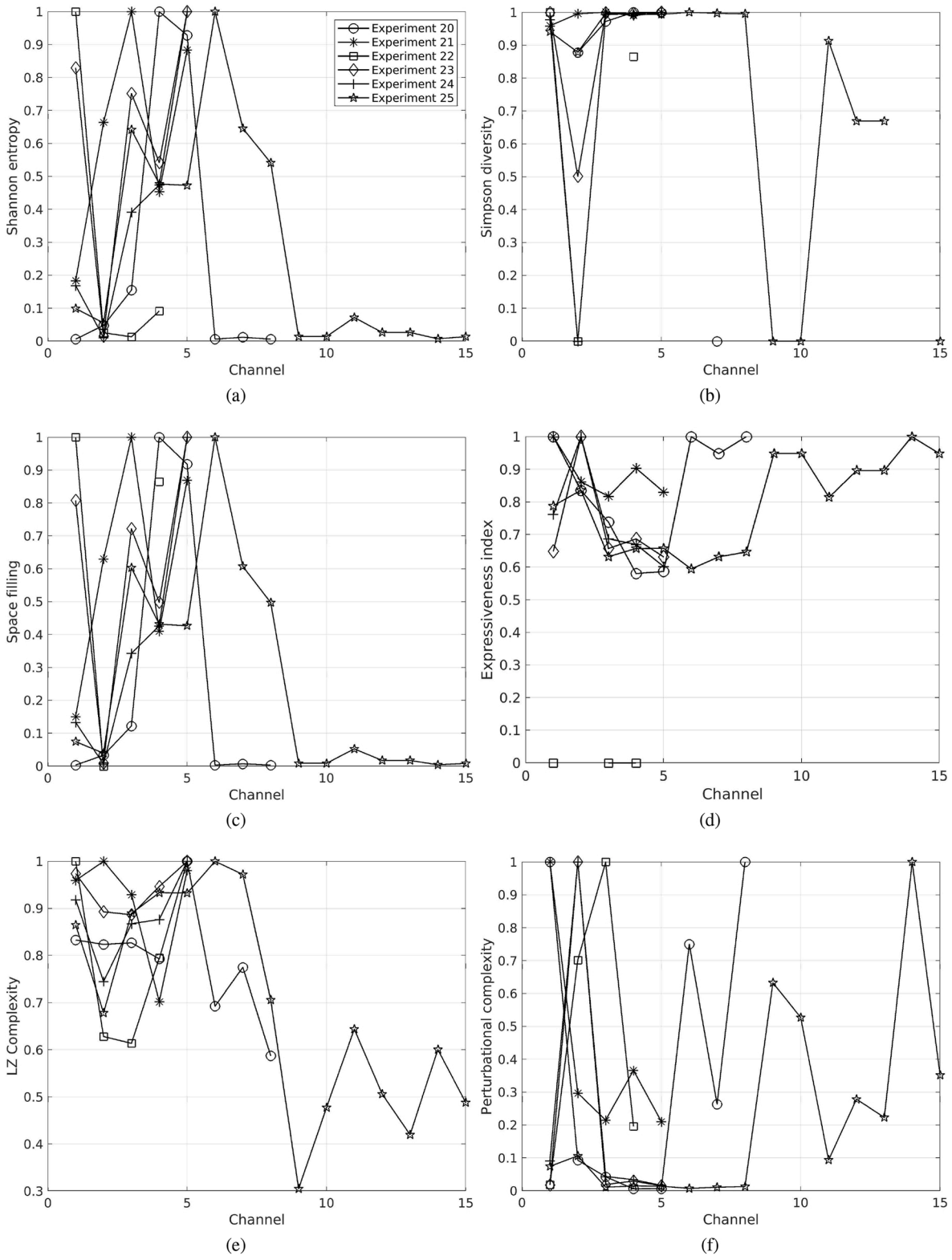


**Fig. 16.** (a) Shannon entropy, (b) Simpson's diversity, (c) Space filling, (d) Expressiveness, (e) Lempel–Ziv complexity, and (f) Perturbation complexity index. All measurements are scaled to the range of $[0, 1]$.

detection method compared to conventional spike detection techniques in neuroscience Nenadic and Burdick (2004); Shimazaki and Shinomoto (2010). We also compared the proposed method with the expert opinion on the location of spikes. In the complexity analysis, we selected the complexity measures used in previous studies Minoofam et al. (2012, 2014); Parsa et al. (2017); Taghipour et al. (2016); Dehshibi et al. (2015, 2020); Gholami et al. (2020) to quantify spatio-temporal activity patterns.

### 4.1. Objective analysis

Various methods have been proposed for detecting and sorting spike

**Table 2**
The mean of complexity measurements for six experiments.

| | #Channel | #Spike | Lempel–Ziv complexity | Shannon entropy | Simpson's diversity | Space filling | Kolmogorov | PCI | Expressiveness |
|---|---|---|---|---|---|---|---|---|---|
| #1 | 8 | 565 | 0.79 | 45.81 | 0.76 | $30.68 \times 10^{-5}$ | $30.36 \times 10^{-4}$ | 0.365 | $20.8 \times 10^{4}$ |
| #2 | 5 | 447 | 0.91 | 63.27 | 0.98 | $35.20 \times 10^{-5}$ | $35.78 \times 10^{-4}$ | 0.021 | $18.6 \times 10^{4}$ |
| #3 | 4 | 124 | 0.75 | 22.57 | 0.61 | $48.10 \times 10^{-5}$ | $10.94 \times 10^{-4}$ | 0.333 | 29.71 |
| #4 | 5 | 951 | 0.93 | 123.11 | 0.89 | $57.30 \times 10^{-5}$ | $56.05 \times 10^{-4}$ | 0.072 | $23.8 \times 10^{4}$ |
| #5 | 5 | 573 | 0.88 | 75.75 | 0.79 | $53.02 \times 10^{-5}$ | $52.80 \times 10^{-4}$ | 0.077 | $16.4 \times 10^{4}$ |
| #6 | 15 | 862 | 0.69 | 39.96 | 0.71 | $24.20 \times 10^{-5}$ | $25.06 \times 10^{-4}$ | 0.207 | $20.4 \times 10^{4}$ |

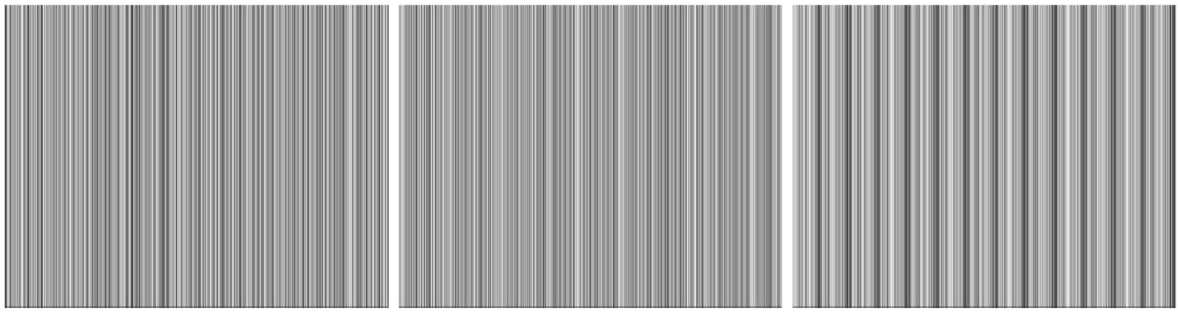


**Fig. 17.** Binary representation of (a) pieces of news,(b) random sequence of alphanumeric, and (c) periodic sequence of alphanumeric after applying Huffman coding.

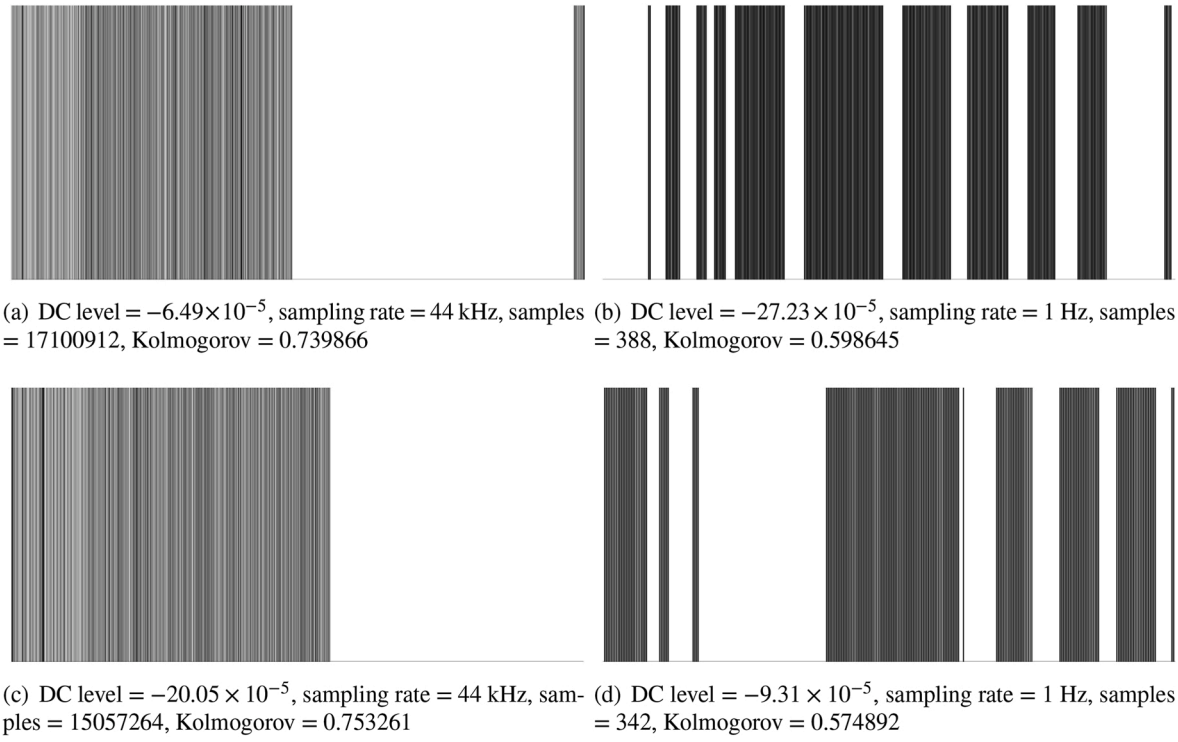


**Fig. 18.** Comparison of the human voice in (a–c) English/Chinese with the electrical activity of fungi with the duration of (b–d) 388/342 s.

events in EC recordings Quiroga et al. (2004); Nenadic and Burdick (2004); Obeid and Wolf (2004); Wilson and Emerson (2002); Gotman and Wang (1991); Wilson et al. (1999); Franke et al. (2010); Rácz et al. (2020); Wang et al. (2020); Sablok et al. (2020); Liu et al. (2020). However, only a few of these methods do not require additional details, such as template construction and the supervised setting of thresholds for detecting and sorting spike events Nenadic and Burdick (2004); Shimazaki and Shinomoto (2010). Nenadic and Burdick Nenadic and Burdick (2004) have developed an unsupervised method for detecting and locating spikes in noisy neural recordings. This approach benefits from the continuous transformation of the wavelet. They applied multi-scale signal decomposition using the 'bior1.3,' 'bior1.5,' 'Haar,' or 'db2' wavelet basis. To determine the presence of spikes, they separated the signal and noise at each scale and performed Bayesian hypothesis

**Table 3**
The complexity measurements for pieces of news, a random sequence of alphanumeric, a periodic sequence of alphanumeric along with three chunks randomly selected from our experiments.

| | Length | Lempel–Ziv complexity | Shannon Entropy | Simpson's diversity | Space filling | Kolmogorov | PCI | Expressiveness |
|---|---|---|---|---|---|---|---|---|
| News | 36187 | 0.127919 | 4.421728 | 0.999941 | 0.465996 | 0.765382 | 0.173096 | 9.49 |
| Random sequence | 36002 | 0.125465 | 5.770331 | 0.999941 | 0.469835 | 1.001850 | 0.173621 | 12.28 |
| Periodic sequence | 36006 | 0.127090 | 3.882058 | 0.999937 | 0.442426 | 0.076508 | 0.019708 | 8.77 |
| Chunk 1 | 36000 | 0.067611 | 16.194914 | 0.947368 | 0.000556 | 0.006307 | 0.000389 | 29150.84 |
| Chunk 2 | 36000 | 0.007250 | 15.478087 | 0.944444 | 0.000528 | 0.006727 | 0.000435 | 29326.90 |
| Chunk 3 | 36000 | 0.068417 | 31.680374 | 0.976190 | 0.001194 | 0.012613 | 0.000398 | 26523.10 |

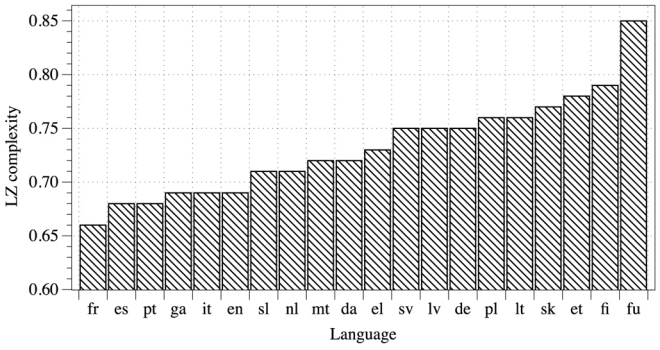


**Fig. 19.** Lempel-Ziv complexity of European languages (data from Sadeniemi et al. (2008)) with average complexity of fungal ('fu') electrical activity language added.

testing. Finally, they combined decisions on different scales to estimate the arrival times of individual spikes.

**Algorithm 3**. Detecting candidate spike region from signal envelope.

Shimazaki and Shinomoto Shimazaki and Shinomoto (2010) proposed an optimisation technique for the timing-histogram bin width selection. This optimisation minimised the mean integrated square in the kernel density estimation. This method benefits from variable kernel width, which allowed grasping non-stationary phenomena. Also, this method used stiffness constant to avoid possible overfitting due to excessive freedom in the bandwidth variability. The calculated bandwidth was then used as a proxy for filtering spike event regions. Fig. 10 shows the results of applying these methods to two chunks with a length of 3000 s.

Both compete methods could not correctly detect all spike events that were located by the expert. The wavelet-based method could locate three spikes in Fig. 10(b) without detecting any spike in Fig. 10(a). The adaptive bandwidth kernel-based method could detect one spike in Fig. 10(b) and one pseudo-spike in Fig. 10(a and b). While our proposed method misidentified one spike event in Fig. 9(a) and three spikes in Fig. 9(b).

We also compared the proposed method with the expert opinion on a randomly selected 36,000-s chunk, i.e., 10 h of electrical activity

**Algorithm 3:** Detecting candidate spike region from signal envelope.

**Input :** $\xi[n]$ — Envelope of signal $L[t]$,
$n_p = 60$ — Minimum distance between two consecutive local extreme.
**Output:** $\mathcal{R}$ — set of envelope-based ROIs.

**begin**
  $\xi_M[n] = \left(\xi_H[n] + \xi_L[n]\right)/2$;
  $[val_{min}, ind_{min}] =$ `isLocalMinimum`$(\xi_M[n], n_p)$;
  $[val_{max}, ind_{max}] =$ `isLocalMaximum`$(\xi_M[n], n_p)$;
  `// isLocalMinimum() and isLocalMaximum() locate local minimum and maximum, respectively.`
  $j \leftarrow$ index of the first local maximum whose value is greater than the value of the first local minimum;
  **for** $i = 1$ **to card**$(ind_{min})$ **do**
    **if** $j \leq$ **card**$(ind_{max})$ **then**
      $\Delta \leftarrow val_{max}(j) - val_{min}(i)$;
      Add $\left(ind_{min}(i), ind_{max}(j), \Delta\right)$ to $\mathcal{R}$;
      $j \leftarrow j + 1$;
    **end**
  **end**
  `//` $\mathcal{R}$ `has` $j$ `rows and 3 columns, as` $\mathcal{R}_1$, $\mathcal{R}_2$, `and` $\mathcal{R}_3$.
  $\rho =$ **mean**$(\mathcal{R}_3) -$ **std**$(\mathcal{R}_3)$;
  `//` **mean**() `and` **std**() `calculate the mean and standard deviation, respectively.`
  Remove the $k^{th}$ entry from $\mathcal{R}$ where $\mathcal{R}_3(k) < \rho$ – see Figure 8(b);
**end**
**return** $\mathcal{R}$

recordings. In this quantitative comparison, the proposed approach could correctly locate 21 spikes and four pseudo-spike events. Our method also overestimated two refractory periods, resulting in the true-positive and false-positive rates of 76% and 16%, respectively. Fig. 11(a) shows located spikes by the expert, and Fig. 11(b) demonstrates the results of the proposed spike detection method.

We applied the proposed method to six experiments where the statistical results are shown in Figs. 12 and 13 and summarised in Table 1. It should be noted that the placement of the electrodes in two experiments was in lines with a distance of 1 cm, in two experiments it was in lines with a distance of 2 cm, and in two experiments it was random with a distance of approximately 2 cm. The proposed method is implemented in MATLAB R2020a, where the code and details of the experiments can be found in Dehshibi and Adamatzky (2020).

**Algorithm 4.** Extracting fungi spike and pseudo-spike events.

**Algorithm 4:** Extracting fungi *spike* and *pseudo-spike* events.

**Input :** $\mathcal{C}, \mathcal{D}, \mathcal{R}$ — Regions of interest.
**Output:** $\mathcal{F}_s, \mathcal{F}_p$ — Fungi *spike* and *pseudo-spike* events, respectively.

**begin**
  **foreach** $r_e \in \mathcal{R}$ **do**
    $chunk_e \leftarrow [r_e^1 \cdots r_e^2]$;
    **foreach** $r_w \in (\mathcal{C} \cup \mathcal{D})$ **do**
      $chunk_w \leftarrow [r_w^1 \cdots r_w^2]$;
      **switch** $chunk_w, chunk_e$ **do**
        **case** $chunk_e \subset chunk_w$ **do**
          $chunk_w(end) = chunk_e(end)$;
          $\mathcal{F}_s \leftarrow chunk_w$;
        **end**
        **case** $chunk_w \subset chunk_e$ **do**
          $\mathcal{F}_p \leftarrow chunk_w$;
        **end**
        **case** `intersect(`$chunk_w, chunk_e$`)` **do**
          `// intersect() checks if two chunks have an intersection point.`
          **Split** the concatenation of $chunk_w$ and $chunk_e$ from intersection point into two *sub-Chunks*;
          $\mathcal{F}_p \leftarrow$ *sub-Chunks*;
        **end**
      **end**
    **end**
  **end**
  **foreach** $r \in (\mathcal{F}_s \cup \mathcal{F}_p)$ **do**
    **Remove** $r$ if $|r| < 60$;
  **end**
**end**
**return** $\mathcal{F}_s, \mathcal{F}_p$

These results are consistent with the experiments carried out on the electrical activity of *Physarum polycephalum* Adamatzky (2013, 2018a) where it has been reported that the length of the Physarum spike is between 60 and 120 s. Physarum is faster than fungi in terms of growth. Now, with further observations, we can hypothesise that the length of the fungal spikes cannot be less than 60 s.

### 4.2. Complexity analysis

To quantify the complexity of the electrical signalling recorded, we used the following measurements:

1. The Shannon entropy ($H$) is calculated as $H = -\sum_{w \in W} (\nu(w)/\eta \cdot ln(\nu(w)/\eta))$, where $\nu(w)$ is a number of times the neighbourhood configuration $w$ is found in configuration $W$, and $\eta$ is the total number of spike events found in all channels of the experiment.
2. Simpson's diversity ($S$) is calculated as $S = \sum_{w \in W} (\nu(w)/\eta)^2$. It linearly correlates with Shannon entropy for $H < 3$ and the relationship becomes logarithmic for higher values of $H$. The value of $S$ ranges between 0 and 1, where 1 represents infinite diversity and 0, no diversity.
3. Space filling ($D$) is the ratio of non-zero entries in $W$ to the total length of string.
4. Expressiveness ($E$) is calculated as the Shannon entropy $H$ divided by space-filling ratio $D$, where it reflects the 'economy of diversity'.
5. Lempel–Ziv complexity ($LZ$) is used to assess temporal signal diversity, i.e., compressibility. Here, we represented the spiking activity of mycelium with a binary string where '1s' indicates the presence of a spike and '0s' otherwise. Formally, as both the barcode and the channels' electrical activity are stored as PNG images, LZ is the ratio of the barcode image size to the size of the electrical activity image (see Figs. 14 and 15).
6. Perturbation complexity index $PCI = LZ/H$.

To calculate Lempel–Ziv complexity, we saved each signal as a PNG image (see two examples in Fig. 15), where the 'deflation' algorithm used in PNG lossless compression Deutsch and Gailly (1996); Howard (1993); Roelofs and Koman (1999) is a variation of the classical LZ77 algorithm Ziv and Lempel (1977). We employed this approach as the recorded signal is a non-binary string. We take the largest PNG file size to normalise this measurement.

In order to assess signal diversity across all channels and observa-

tions, each experiment was represented by a binary matrix with a row for each channel and a column for each observation. This binary matrix is then concatenated by observation to form a single binary string. We used Kolmogorov complexity algorithm Kaspar and Schuster (1987) to measure the Lempel—-Ziv complexity (*LZc*) across channels. *LZc* captures both temporal diversity on a single channel and spatial diversity across channels. We also normalised *LZc* by dividing the raw value by the randomly shuffled value obtained for the same binary input sequence. Since the value of *LZ* for a fixed-length binary sequence is maximum if the sequence is absolutely random, the normalised values represent the degree of signal diversity on a scale from 0 to 1. The results of the calculation of these complexity measurements for all six configurations are shown in Fig. 16 and summarised in Table 2.

We calculated the aforementioned complexity criteria for three forms of writing to illustrate the communication complexity of the mycelium substrate, including (1) news items,[3] (2) random alphanumeric sequences[4] and (3) periodic alphanumeric sequences encoded with Huffman code Huffman (1952), see barcode in Fig. 17. Table 3 presents the results of the comparison. We also considered two podcasts in English (387 s) and Chinese (385 s) to compare the complexity of fungal spiking with human speech. Both podcasts were in MP3 format at a sampling rate of 44100 Hz. We randomly selected two chunks from two electrical activity channels with a duration of 388 and 342 s to compare with the English and Chinese podcasts, respectively. We observed that, in both cases, the Kolmogorov complexity of the fungal is lower than the human speech, implying the fact that the amount of information transmitted by the fungi is less than the human voice. From a technical point of view, we computed the DC level of each signal and binarised the signal with respect to that level Huang and Lin (2009). To binaries the signal, we set the inputs with values less than or equal to the DC level to 0 and the rest of the inputs to 1. The findings are shown in Fig. 18.

## 6. Discussion

We developed algorithmic framework for exhaustive characterisation of electrical activity of a substrate colonised by mycelium of oyster fungi *Pleurotus djamor*. We evidenced spiking activity of the mycelium. We found that average dominant duration of an action-potential like spike is 402 s. The spikes amplitudes' depends on the location of the source of electrical activity related to the position of electrodes, thus the amplitudes provide less useful information. The amplitudes vary from 0.5 mV to 6 mV. This is indeed low compared to 50–60 mV of intracellular recording, nevertheless understandable due to the fact the electrodes are inserted not even in mycelium strands but in the substrate colonised by mycelium. The shift of the distribution to higher values of spike amplitude in experiments with a distance of 2 cm between the electrodes might indicate that the width of the propagation of the excitation wave front exceeds 1 cm and might even be close to 2 cm.

The spiking events have been characterised with several complexity measures. Most measures, apart of Kolmogorov complexity shown a low degree of variability between channels (different sites of the recordings). The Kolmogorov complexity of fungal spiking varies from $11\times 10^{-4}$ to $57\times 10^{-4}$. This might indicated mycelium sub-networks in different parts of the substrate have been transmitting different information to other parts of the mycelium network. This is somehow echoes experimental results on communication between ants analysed with Kolmogorov complexity: longer paths communicated ants corresponds to higher values of complexity Ryabko and Reznikova (1996).

LZ complexity of fungal language (Table 2) is much higher than of news, random or periodic sequences (Table 3). The same can be observed for Shannon entropy. Kolmogorov complexity of the fungal language is much lower than that of news sampler or random or periodic sequences. Complexity of European languages based on their compressibility Sadeniemi et al. (2008) is shown in Fig. 19, French having lowest LZ complexity 0.66 and Finnish highest LZ complexity 0.79. Fungal language of electrical activity has minimum LZ complexity 0.61 and maximum 0.91 (media 0.85, average 0.83). Thus, we can speculate that a complexity of fungal language is higher than that of human languages (at least for European languages).

[3] https://www.sciencemag.org/news/2020/07/meet-lizard-man-reptile-loving-biologist-tackling-some-biggest-questions-evolution.

[4] We used available service at https://www.random.org/.

## Credit author statement

All authors are responsible for the experiments and writing of the paper.

## Declaration of competing interest

There is no conflict of interest with this paper.

## Acknowledgement

This project has received funding from the European Union's Horizon 2020 research and innovation programme FET OPEN "Challenging current thinking" under grant agreement No 858132.

## References

Adamatzky, A., 2013. Tactile bristle sensors made with slime mold. IEEE Sensor. J. 14, 324–332.
Adamatzky, A., 2018a. On spiking behaviour of oyster fungi Pleurotus djamor. Sci. Rep. 8, 1–7.
Adamatzky, A., 2018b. Towards fungal computer. Interface focus 8, 20180029.
Adamatzky, A., 2019. Plant leaf computing. Biosystems 182, 59–64.
Adamatzky, A., Chiolerio, A., Sirakoulis, G., 2021. Electrical resistive spiking of fungi. Biophys. Rev. Lett. 1–7. https://doi.org/10.1142/S1793048021500016, 0.
Adamatzky, A., Nikolaidou, A., Gandia, A., Chiolerio, A., Dehshibi, M.M., 2020. Reactive fungal wearable. Biosystems 199, 104304.
Aidley, D.J., Ashley, D., 1998. The Physiology of Excitable Cells, vol. 4. Cambridge University Press, Cambridge.
Belousov, B.P., 1959. A periodic reaction and its mechanism. Compilation of Abstracts on Radiation Medicine 147, 1.
Bingley, M., 1966. Membrane potentials in amoeba proteus. J. Exp. Biol. 45, 251–267.
Davidenko, J.M., Pertsov, A.V., Salomonsz, R., Baxter, W., Jalife, J., 1992. Stationary and drifting spiral waves of excitation in isolated cardiac muscle. Nature 355, 349.
Dehshibi, M.M., Adamatzky, A., 2020. Supplementary Material for "Electrical Activity of Fungi: Spikes Detection and Complexity Analysis" https://doi.org/10.5281/zenodo.3997031. (Accessed 24 August 2020).
Dehshibi, M.M., Shanbehzadeh, J., Pedram, M.M., 2020. A robust image-based cryptology scheme based on cellular nonlinear network and local image descriptors. Int. J. Parallel, Emergent Distributed Syst. 35, 514–534.
Dehshibi, M.M., Shirmohammadi, A., Adamatzky, A., 2015. On growing Persian words with l-systems: visual modeling of neyname. Int. J. Image Graph. 15, 1550011.
Deutsch, P., Gailly, J., 1996. Zlib Compressed Data Format Specification Version 3.3. Technical Report. RFC 1950. May.
Eckert, R., Brehm, P., 1979. Ionic mechanisms of excitation in paramecium. Annu. Rev. Biophys. Bioeng. 8, 353–383.
Farkas, I., Helbing, D., Vicsek, T., 2002. Social behaviour: Mexican waves in an excitable medium. Nature 419, 131.
Farkas, I., Helbing, D., Vicsek, T., 2003. Human waves in stadiums. Phys. Stat. Mech. Appl. 330, 18–24.
Franke, F., Natora, M., Boucsein, C., Munk, M.H., Obermayer, K., 2010. An online spike detection and spike classification algorithm capable of instantaneous resolution of overlapping spikes. J. Comput. Neurosci. 29, 127–148.
Fromm, J., Lautner, S., 2007. Electrical signals and their physiological significance in plants. Plant Cell Environ. 30, 249–257.
Gholami, N., Dehshibi, M.M., Adamatzky, A., Rueda-Toicen, A., Zenil, H., Fazlali, M., Masip, D., 2020. A novel method for reconstructing ct images in gate/geant4 with application in medical imaging: a complexity analysis approach. J. Inf. Process. 28, 161–168.
Gorbunov, L., Kirsanov, V., 1987. Excitation of plasma waves by an electromagnetic wave packet. Sov. Phys. JETP 66, 40.
Gotman, J., Wang, L., 1991. State-dependent spike detection: concepts and preliminary results. Electroencephalogr. Clin. Neurophysiol. 79, 11–19.
Hall, C.A., Meyer, W.W., 1976. Optimal error bounds for cubic spline interpolation. J. Approx. Theor. 16, 105–122.
Hansma, H.G., 1979. Sodium uptake and membrane excitation in paramecium. J. Cell Biol. 81, 374–381.

Hodgkin, A.L., Huxley, A.F., 1952. A quantitative description of membrane current and its application to conduction and excitation in nerve. J. Physiol. 117, 500–544.
Howard, P.G., 1993. The Design and Analysis of Efficient Lossless Data Compression Systems. Ph.D. thesis. Citeseer.
Huang, H., Lin, F., 2009. A speech feature extraction method using complexity measure for voice activity detection in wgn. Speech Commun. 51, 714–723.
Huffman, D.A., 1952. A method for the construction of minimum-redundancy codes. Proceedings of the IRE 40, 1098–1101.
IEEE, 2011. Ieee Standard for Transitions, Pulses, and Related Waveforms. IEEE Std 181-2011 (Revision of IEEE Std 181-2003) , 1–71doi. https://doi.org/10.1109/IEEESTD.2011.6016198.
Kaspar, F., Schuster, H., 1987. Easily calculable measure for the complexity of spatiotemporal patterns. Phys. Rev. A 36, 842.
Kittel, C., 1958. Excitation of spin waves in a ferromagnet by a uniform rf field. Phys. Rev. 110, 1295.
Lilly, J.M., 2017. Element analysis: a wavelet-based method for analysing time-localized events in noisy time series. Proc. Math. Phys. Eng. Sci. 473, 20160776.
Lilly, J.M., Olhede, S.C., 2008. Higher-order properties of analytic wavelets. IEEE Trans. Signal Process. 57, 146–160.
Lilly, J.M., Olhede, S.C., 2012. Generalized morse wavelets as a superfamily of analytic wavelets. IEEE Trans. Signal Process. 60, 6036–6041.
Liu, Z., Wang, X., Yuan, Q., 2020. Robust detection of neural spikes using sparse coding based features. Math. Biosci. Eng. 17, 4257.
Marple, L., 1999. Computing the discrete-time" analytic" signal via fft. IEEE Trans. Signal Process. 47, 2600–2603.
Masi, E., Ciszak, M., Santopolo, L., Frascella, A., Giovannetti, L., Marchi, E., Viti, C., Mancuso, S., 2015. Electrical spiking in bacterial biofilms. J. R. Soc. Interface 12, 20141036.
McGillviray, A.M., Gow, N.A., 1987. The transhyphal electrical current of *Neuruspua crassa* is carried principally by protons. Microbiology 133, 2875–2881.
Minoofam, S.A.H., Dehshibi, M.M., Bastanfard, A., Eftekhari, P., 2012. Ad-hoc ma'qeli script generation using block cellular automata. J. Cell. Automata 7, 321–334.
Minoofam, S.A.H., Dehshibi, M.M., Bastanfard, A., Shanbehzadeh, J., 2014. Pattern formation using cellular automata and l-systems: a case study in producing islamic patterns. In: Cellular Automata in Image Processing and Geometry. Springer, pp. 233–252.
Nelson, P.G., Lieberman, M., 2012. Excitable Cells in Tissue Culture. Springer Science & Business Media.
Nenadic, Z., Burdick, J.W., 2004. Spike detection using the continuous wavelet transform. IEEE Trans. Biomed. Eng. 52, 74–87.
Obeid, I., Wolf, P.D., 2004. Evaluation of spike-detection algorithms fora brain-machine interface application. IEEE (Inst. Electr. Electron. Eng.) Trans. Biomed. Eng. 51, 905–911.
Parsa, S.S., Sourizaei, M., Dehshibi, M.M., Shateri, R.E., Parsaei, M.R., 2017. Coarse-grained correspondence-based ancient sasanian coin classification by fusion of local features and sparse representation-based classifier. Multimed. Tool. Appl. 76, 15535–15560.
Quiroga, R.Q., Nadasdy, Z., Ben-Shaul, Y., 2004. Unsupervised spike detection and sorting with wavelets and superparamagnetic clustering. Neural Comput. 16, 1661–1687.
Rácz, M., Liber, C., Németh, E., Fiáth, R., Rokai, J., Harmati, I., Ulbert, I., Márton, G., 2020. Spike detection and sorting with deep learning. J. Neural. Eng. 17, 016038.
Roelofs, G., Koman, R., 1999. PNG: the Definitive Guide. O'Reilly & Associates, Inc.
Ryabko, B., Reznikova, Z., 1996. Using shannon entropy and Kolmogorov complexity to study the communicative system and cognitive capacities in ants. Complexity 2, 37–42.
Sablok, S., Gururaj, G., Shaikh, N., Shiksha, I., Choudhary, A.R., 2020. Interictal spike detection in eeg using time series classification. In: 2020 4th International Conference on Intelligent Computing and Control Systems (ICICCS). IEEE, pp. 644–647.
Sadeniemi, M., Kettunen, K., Lindh-Knuutila, T., Honkela, T., 2008. Complexity of European Union languages: a comparative approach. J. Quant. Ling. 15, 185–211.
Shimazaki, H., Shinomoto, S., 2010. Kernel bandwidth optimization in spike rate estimation. J. Comput. Neurosci. 29, 171–182.
Slonczewski, J., 1999. Excitation of spin waves by an electric current. J. Magn. Magn Mater. 195, L261–L268.
Taghipour, N., Javadi, H.H.S., Dehshibi, M.M., Adamatzky, A., 2016. On complexity of Persian orthography: L-systems approach. Complex Syst. 25, 127–156.
Trebacz, K., Dziubinska, H., Krol, E., 2006. Electrical signals in long-distance communication in plants. In: Communication in Plants. Springer, pp. 277–290.
Tsoi, M., Jansen, A., Bass, J., Chiang, W.C., Seck, M., Tsoi, V., Wyder, P., 1998. Excitation of a magnetic multilayer by an electric current. Phys. Rev. Lett. 80, 4281.
Vicnesh, J., Hagiwara, Y., 2019. Accurate detection of seizure using nonlinear parameters extracted from eeg signals. J. Mech. Med. Biol. 19, 1940004.
Wang, Z., Wu, D., Dong, F., Cao, J., Jiang, T., Liu, J., 2020. A novel spike detection algorithm based on multi-channel of bect eeg signals. IEEE Transactions on Circuits and Systems II: Express Briefs.
Wilson, S.B., Emerson, R., 2002. Spike detection: a review and comparison of algorithms. Clin. Neurophysiol. 113, 1873–1881.
Wilson, S.B., Turner, C.A., Emerson, R.G., Scheuer, M.L., 1999. Spike detection ii: automatic, perception-based detection and clustering. Clin. Neurophysiol. 110, 404–411.
Zhabotinsky, A., 1964. Periodic processes of malonic acid oxidation in a liquid phase. Biofizika 9, 11.
Zhabotinsky, A.M., 2007. Belousov-zhabotinsky reaction. Scholarpedia 2, 1435.
Zimmermann, M.R., Mithöfer, A., 2013. Electrical long-distance signaling in plants. In: Long-Distance Systemic Signaling and Communication in Plants. Springer, pp. 291–308.
Ziv, J., Lempel, A., 1977. A universal algorithm for sequential data compression. IEEE Trans. Inf. Theor. 23, 337–343.

**Mohammad Mahdi Dehshibi** received his PhD in Computer Science from Islamic Azad University, Tehran, Iran in 2017. He is currently a postdoctoral research fellow at Universitat Oberta de Catalunya (UOC). He was a visiting researcher in Unconventional Computing Lab, UWE, Bristol, U.K. He has contributed to over 50 papers published in scientific Journals or International Conferences. His research interests include Unconventional Computing, Affective Computing, and Cellular Automata.

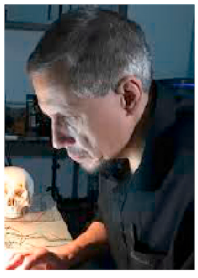

**Andrew Adamatzky** is Professor of Unconventional Computing and Director of the Unconventional Computing Laboratory, Department of Computer Science, University of the West of England, Bristol, UK. He does research in molecular computing, reaction-diffusion computing, collision-based computing, cellular automata, slime mould computing, massive parallel computation, applied mathematics, complexity, nature-inspired optimisation, collective intelligence and robotics, bionics, computational psychology, nonlinear science, novel hardware, and future and emergent computation. He authored seven books, mostly notable are 'Reaction-Diffusion Computing', 'Dynamics of Crow Minds', 'Physarum Machines', and edited twenty-two books in computing, most notable are 'Collision Based Computing', 'Game of Life Cellular Automata', 'Memristor Networks'; he also produced a series of influential artworks published in the atlas 'Silence of Slime Mould'. He is founding editor-in-chief of 'J of Cellular Automata' and 'J of Unconventional Computing' and editor-in-chief of 'J Parallel, Emergent, Distributed Systems' and 'Parallel Processing Letters'.